

# Structure of the (0001) basal twin boundary in $\text{Bi}_2\text{Te}_3$

D. L. Medlin,<sup>1,a)</sup> Q. M. Ramasse,<sup>2,b)</sup> C. D. Spataru,<sup>1</sup> and N. Y. C. Yang<sup>1</sup><sup>1</sup>Sandia National Laboratories, Livermore, California 94551, USA<sup>2</sup>National Center for Electron Microscopy, Lawrence Berkeley National Laboratory, Berkeley, California 94720, USA

(Received 31 March 2010; accepted 3 June 2010; published online 24 August 2010)

We investigate the structure of the (0001) basal twin boundary in  $\text{Bi}_2\text{Te}_3$ . Electron diffraction measurements show that this interface corresponds to a  $180^\circ$  rotation of the crystal about the [0001] axis, an alignment that reverses the stacking of the basal planes. The basal planes in the perfect  $\text{Bi}_2\text{Te}_3$  structure are arranged in a repeating sequence of five-layer wide  $\text{Te}^{(1)}\text{--Bi--Te}^{(2)}\text{--Bi--Te}^{(1)}$  packets. Thus, it is possible for the twin interface to be located at one of three distinct locations: at the  $\text{Te}^{(2)}$  layer, the Bi layer, or the  $\text{Te}^{(1)}$  layer. Using aberration-corrected high-angle annular dark field scanning transmission electron microscopy, we show that the twin boundary is terminated at the  $\text{Te}^{(1)}$  layer, where the stacking forms a double-layer of Te. Our observations are consistent with *ab initio* calculations, which predict this twin termination to have the lowest interfacial energy of the three configurations we considered. Our calculations and observations also find a small expansion in the interplanar spacing at the interface. © 2010 American Institute of Physics. [doi:10.1063/1.3457902]

## I. INTRODUCTION

Thermoelectric devices based on bismuth telluride ( $\text{Bi}_2\text{Te}_3$ ) are widely used for both cooling and power generation. Applications include Peltier coolers for refrigeration and thermal management of electronic and optical components, and thermopiles for direct thermal to electrical conversion from waste-heat, ambient thermal sources, and radioisotopes.<sup>1</sup> In practice,  $\text{Bi}_2\text{Te}_3$ -based devices typically employ polycrystalline materials that are solid solution alloys of  $\text{Bi}_2\text{Te}_3$  with the isomorphous compounds  $\text{Sb}_2\text{Te}_3$  and  $\text{Bi}_2\text{Se}_3$ .<sup>2</sup>

The energy conversion efficiency of a thermoelectric material is typically characterized in terms of its thermoelectric figure-of-merit,  $zT = \alpha^2 \sigma T / \kappa$ , where  $\alpha$  is the Seebeck coefficient,  $\sigma$  is the electrical conductivity,  $\kappa$  is the thermal conductivity, and  $T$  is temperature. Grain boundaries in thermoelectric materials are important because they can affect  $zT$  through the scattering of electronic carriers and phonons. Significant improvements in the performance of bulk  $\text{Bi}_2\text{Te}_3$ -based materials have been achieved by reducing the grain size to nanoscale dimensions, giving  $zT$ 's between 1.4–1.6 (Refs. 3 and 4) (versus  $zT \sim 1$  in conventional materials). This improved performance results largely from reductions in  $\kappa$  due to increased phonon scattering at the high density of embedded interfaces. In principle, such nanostructured materials could be further improved if the grain boundaries could be specifically engineered to optimize electronic properties in addition to blocking phonons.<sup>5</sup> However, at present, our limited knowledge of even basic details of the structure and composition of grain boundaries in  $\text{Bi}_2\text{Te}_3$  makes achieving this goal difficult.

Because of their high symmetry, twin boundaries are perhaps the simplest possible grain boundary, making them a useful starting point for the analysis of more general interfaces in  $\text{Bi}_2\text{Te}_3$  and its alloys. Moreover, twin boundaries are of particular interest because their near bulk-like atomic-coordination can yield favorable electronic transport properties. For example, {111} twins in silicon exhibit lower potential barriers<sup>6</sup> and are less electrically active<sup>7,8</sup> than more general, random boundaries. Similarly, Cook *et al.*<sup>9</sup> have shown that the presence of high twin densities in the thermoelectric compound  $(\text{AgSbTe}_2)_{15}(\text{GeTe})_{85}$  (TAGS-85) does not degrade the electrical conductivity in this material. This behavior of twin boundaries may be advantageous for thermoelectric materials where one desires interfaces that can scatter phonons while not degrading the electronic properties.<sup>10</sup>

In this paper, we investigate the structure of the (0001) basal twin boundary in  $\text{Bi}_2\text{Te}_3$ . In general, twins can form during initial growth, deformation, or subsequent annealing.<sup>11,12</sup>  $\text{Bi}_2\text{Te}_3$ -based thermoelectric materials often undergo extensive deformation during processing to refine the grain size and to control the crystallographic texture for optimal thermal and electronic transport,<sup>10,13–17</sup> potentially leading to twin formation. For instance, (0001) twins in  $\text{Bi}_2\text{Te}_3/\text{Sb}_2\text{Te}_3$  bulk nanocomposites were observed by Cao *et al.*<sup>18</sup> who attributed their formation to shear deformation during the hot-pressing stage of sample consolidation. Lamellar features with a blocky termination suggestive of growth or annealing twins are also apparent in the micrographs of hot-pressed nanocrystalline  $(\text{Bi}, \text{Sb})_2\text{Te}_3$  presented by Poudel *et al.*<sup>3</sup>

$\text{Bi}_2\text{Te}_3$  has a rhombohedral crystal structure<sup>19</sup> ( $R\bar{3}m$ ) that is commonly indexed in terms of an hexagonal cell with lattice parameters  $a=0.438$  nm and  $c=3.050$  nm.<sup>20,21</sup> This structure consists of alternating layers of Te and Bi that are arranged along the  $c$ -axis in five-layer packets or “quintets”

a)Electronic mail: dlmedli@sandia.gov

b)Present address: SuperSTEM Laboratory, STFC Daresbury, Daresbury WA4 4AD, UK.



(...:Te<sup>(1)</sup>–Bi–Te<sup>(2)</sup>–Bi–Te<sup>(1)</sup>::Te<sup>(1)</sup>–Bi–Te<sup>(2)</sup>–Bi–Te<sup>(1)</sup>:...). As we discuss in more detail below, the (0001) basal twin results from a reversal in the stacking sequence of these layers. The question that we address in this paper is at what compositional layer does this reversal occur? To answer this question we investigate the atomic-scale interfacial structure of the twin using transmission electron microscopy (TEM) and compare these observations with the predictions of *ab initio* calculations.

## II. EXPERIMENTAL AND COMPUTATIONAL METHODS

Our observations were conducted on polycrystalline Bi<sub>2</sub>Te<sub>3</sub>. This material was prepared from pure Bi<sub>2</sub>Te<sub>3</sub> powder (~99.99%) (Cerac) and consolidated by spark plasma sintering (SPS). Before consolidation, the powder was reduced to 200 nm from its initial nominal size of 10 μm by mechanical milling. The milling was done in a planetary ball mill for 4 h under a nitrogen atmosphere using stainless steel vessels and tempered steel balls. The SPS consolidation was conducted under an axial compressive pressure of 50 MPa at 673 K in an SPSS-825 apparatus (SPS Syntex Inc., Kanagawa, Japan). We employed a cylindrical graphite die with an inner diameter of 14 mm, using two graphite plungers of the same size to seal the die on both ends and to transfer the load during consolidation. The temperature ramping rate was 50 K/min and the holding time was 3 min.

Specimens for TEM were prepared by mechanical dimpling followed by Ar<sup>+</sup> ion milling (Fischione, Model 1010). In our previous work on PbTe,<sup>22</sup> we have found that specimen damage can arise if the ion-milling conditions are not carefully controlled. Similar damage can arise in Bi<sub>2</sub>Te<sub>3</sub>-based materials, with the signature appearance of dense striations, visible in bright field TEM, with spacings on the order of 10 nm. These features are not associated with any crystallographic reorientation and are distinct from twins. To avoid such artifacts in the present study, we used a liquid N<sub>2</sub>-cooled stage and low-angle, low-energy conditions for the ion-milling. Specifically, the stage temperature was kept to less than 173 K and the accelerating voltage, current, and angle of incidence ( $\theta$ ) of the ions were adjusted as follows: (i) initial milling to perforation:  $\theta=10^\circ$ , 4.5 kV, and 5.0 mA; (ii) enlargement of perforation:  $\theta=8^\circ$ , 3.0 kV, and 5.0 mA; and (iii) final polishing:  $\theta=6^\circ$ , 1.0 kV, and 3.0 mA.

Conventional TEM observations were conducted using a JEOL 2010F instrument operated at an acceleration voltage of 200 kV. To investigate the interfacial atomic structure, we employed high-angle annular dark field (HAADF) scanning TEM (STEM), using the aberration corrected TEAM 0.5 microscope at the National Center for Electron Microscopy (LBNL, Berkeley CA, USA). This instrument is an improved FEI Titan microscope possessing an advanced STEM corrector capable of forming electron probes as small as 0.05 nm at 300 kV acceleration voltage.<sup>23</sup> Great care was taken to characterize all instrumental parameters, including the detector size (65–350 mrad semiangles), electron wave aberrations up to fifth order, as well as the chromatic aberration coefficient

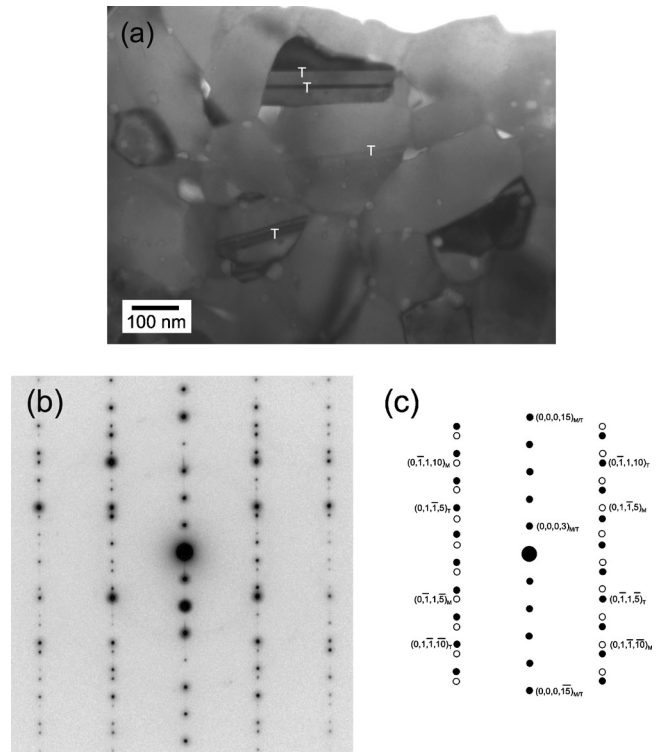


FIG. 1. (a) Bright field TEM image showing grain structure in the Bi<sub>2</sub>Te<sub>3</sub> material. Twins (marked with T) are visible traversing the grains. (b)  $[2\bar{1}10]_M/[2110]_T$  selected area electron diffraction pattern, and its indexing (c), for matrix and twin. Matrix reflections are indicated in white; twin reflections in black. Pattern is taken from the upper grain in (a).

( $C_c=1.0$  mm) and energy spread ( $\Delta E=0.9$  eV), so that these parameters could be used in further analyses.

The *ab initio* calculations for this study were performed using the density functional theory (DFT) formalism with the local-density approximation (LDA) for the exchange correlation potential.<sup>24</sup> We employed a plane-wave basis set including plane waves up to a cutoff energy of 100 Ry. The electron-ion interaction was modeled using the first-principles norm-conserving pseudopotentials of Troullier–Martins.<sup>25</sup> The 4*f* and 5*d* states of Bi and the 4*d* states of Te were frozen into the core. Partial core corrections,<sup>26</sup> as well as scalar relativistic corrections, were also introduced. We did not include spin-orbit interaction effects, as we do not expect them to be important for the ionic optimization. Each twin structure was accommodated in a 30 atom hexagonal supercell. To allow periodic boundary conditions along the *c*-axis, each supercell was constructed with two structurally identical, but oppositely oriented, twin boundaries. The Brillouin zone was sampled using a  $7 \times 7 \times 1$  Monkhorst–Pack grid.<sup>27</sup>

## III. RESULTS

Figure 1 shows a TEM micrograph of the typical polycrystalline microstructure of the Bi<sub>2</sub>Te<sub>3</sub> material. Twin boundaries can be seen as linear features traversing the grains. Analysis of selected area electron diffraction patterns from such twins [Figs. 1(b) and 1(c)] establishes that the twin orientation relationship is  $(0001)_M/(0001)_T$  and



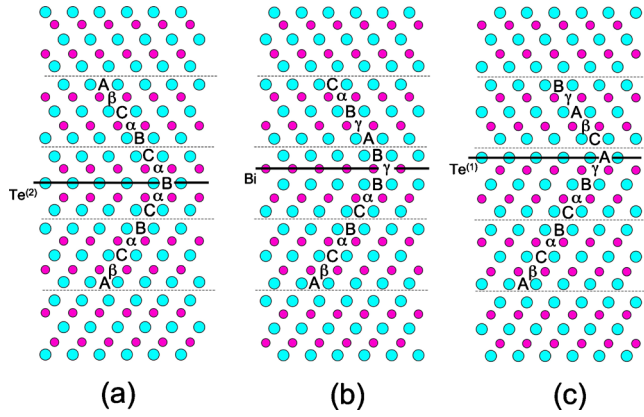


FIG. 2. (Color online) Relaxed structures for the three twin terminations obtained from the *ab initio* calculations. Structures are projected along a  $[2\bar{1}\bar{1}0]$  direction. Bi atoms are indicated by small magenta circles; Te atoms are indicated by large blue circles. The stacking arrangements, as discussed in the text, are indicated by Greek (Bi) and Roman (Te) characters. (a) Twin 1: terminated at a  $\text{Te}^{(2)}$  layer. (b) Twin 2: terminated at a Bi layer. (c) Twin 3: terminated at  $\text{Te}^{(1)}$  layer. Only Twin 1 is mirror symmetric about the interface plane.

$[\bar{2}1\bar{1}0]_M / [\bar{2}1\bar{1}0]_T$ , where M and T refer to the matrix and twin, respectively. The habit planes of the twins lie parallel with (0001). This orientation aligns close-packed planes and directions in the two crystals and represents a rotation of the two crystals with respect to each other by  $180^\circ$  about the c-axis—a configuration that is equivalent to reversing the stacking of the basal planes.

Several microscopic possibilities exist for this stacking arrangement. Designating the Bi and Te layers by Greek and Roman letters, respectively, the basal plane stacking of  $\text{Bi}_2\text{Te}_3$  can be compactly represented as<sup>28</sup>

$$\dots A\beta C\alpha B \ C\alpha B \ \gamma A \ B \ \gamma A\beta C \ \dots \quad (1)$$

In this notation, a unit such as  $A\beta C\alpha B$  represents a five-layer,  $\text{Te}^{(1)}\text{--Bi--Te}^{(2)}\text{--Bi--Te}^{(1)}$  quintet; each unit cell consists of three such quintets. Assuming that the twin boundary arises simply as a reversal of the basal plane stacking, with no further interfacial reconstruction, the twin may be terminated in one of three ways: (1) at the  $\text{Te}^{(2)}$  layer in the middle of the five-layer quintet, (2) at a Bi layer, or (3) at the  $\text{Te}^{(1)}$  layer (the Te double-layer). The stacking sequences for these three configurations are (see Fig. 2)

$$\begin{aligned} \text{Twin 1: } & \dots A\beta C\alpha B \ C\alpha \underline{B} \alpha C \ B\alpha C\beta A \ \dots, \\ \text{Twin 2: } & \dots A\beta \ C\alpha B \ C\alpha B \ \underline{\gamma} B \ A \ \gamma B\alpha C \ \dots, \\ \text{Twin 3: } & \dots A\beta C\alpha B \ C\alpha B \ \underline{\gamma A} \ C\beta A \ \gamma B \ \dots, \end{aligned} \quad (2)$$

where the underscore indicates the twin plane. Note that only the first possibility, Twin 1, has mirror symmetry at the boundary plane.

We performed *ab initio* calculations to investigate the interfacial relaxations and energies of these three structures (Fig. 2). We computed the interfacial energies by taking the difference between the energy of each relaxed structure and that of a reference perfect crystal with the same number of atoms and stoichiometry, normalizing this energy to the unit

TABLE I. Calculated interfacial energies for the three  $\text{Bi}_2\text{Te}_3$  (0001) twin structures.

Twin ID	Interface location	Interface energy (mJ/m <sup>2</sup> )
1	$\text{Te}^{(2)}$	60.1
2	Bi	303
3	$\text{Te}^{(1)}$ (Te double-layer)	40.7

cell area in the a-b plane, and dividing by 2 to account for the presence of two interfaces within each supercell. These results are summarized in Table I. The calculations predict that the twin terminated at the Bi layer (Twin 2) has the highest energy, whereas the twin terminated at the  $\text{Te}^{(1)}$  layer (Twin 3) has the lowest energy. The calculations also predict relaxations of the interplanar spacings normal to the interface. For instance, at the interface of Twin 3, the  $\text{Te}^{(1)}\text{--Te}^{(1)}$  interplanar spacing is increased by 0.0120 nm relative to the equivalent spacing in the single crystal. As we discuss below, the relative interfacial energies can be rationalized in terms of the bonding and geometrical distortions for the three structures.

We compared these calculations with experimental observations of the interfacial atomic structure obtained by HAADF-STEM imaging. In such images, the intensity of each atomic column can be directly related to the  $n$ th power ( $n=1.5\text{--}2$ ) of its average atomic number  $Z$  and hence be used as a guide for chemical identification.<sup>29</sup> Because bismuth has a much larger atomic number than tellurium ( $\text{Bi}:Z=83$  and  $\text{Te}:Z=52$ ), the HAADF intensity of the bismuth columns is higher than that of the tellurium columns allowing these elements to be readily distinguished. To make these observations, we aligned each grain of interest along a  $\langle 2\bar{1}\bar{1}0 \rangle$  type zone axis. As illustrated in Fig. 2, in this projection each atomic column consists of only a single type of atom, allowing the stacking sequence of the basal planes to be straightforwardly resolved.

Figure 3 shows a representative HAADF-STEM image of a (0001)  $\text{Bi}_2\text{Te}_3$  twin boundary. In this image, the five-layer quintet structure of the bulk crystal is clearly observed. Based on the relative atomic numbers of the two species and their expected positions in the perfect crystal, we interpret the two rows of bright intensity peaks within each packet as the Bi columns and the three fainter rows of intensity as the Te columns. The twin boundary itself, which is located near the center of the image, can be identified by the reversal of stacking of the (0001) planes. The positions of the double layers of  $\text{Te}^{(1)}$  atoms, can also be distinguished by the larger separation of these planes, which gives rise to a darker band of contrast between every five-layer packet. From examination of the image it is clear that the reversal of stacking occurs between the two fainter intensity peaks, which we interpret as the  $\text{Te}^{(1)}$  double-layer. The atom positions from the relaxed structure of Twin 3 are overlaid on the image in Fig. 3.

To confirm this interpretation, we simulated HAADF-STEM images for the three candidate structures obtained from the *ab initio* calculations (Fig. 4). We employed the



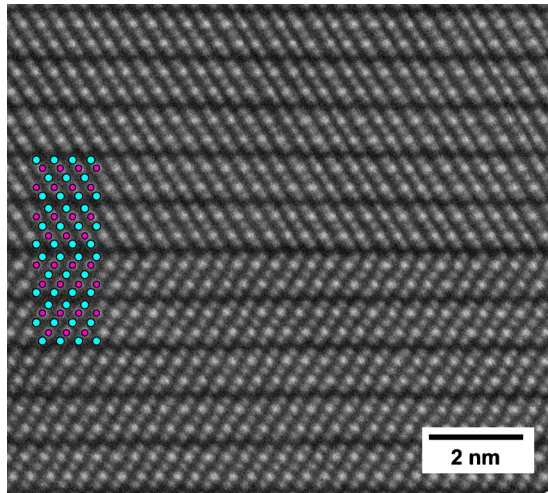


FIG. 3. (Color online) HAADF-STEM image of the (0001) basal twin. Image is projected along  $[2\bar{1}\bar{1}0]$  direction. High intensity peaks correspond to Bi atomic columns; low intensity peaks correspond to Te atomic columns. The image is overlaid with the calculated atom positions of Twin 3. (Large blue circles: Te. Small magenta circles: Bi)

QSTEM software suite<sup>30</sup> using experimental parameters measured for the instrument and specimen. Based on thickness estimates that we derived by analyzing low loss electron energy loss spectra using the log-ratio method,<sup>31</sup> we used a specimen thickness of 39 nm for these calculations. The simulated images can then be quantitatively compared to the experiment using the same color intensity scale representing

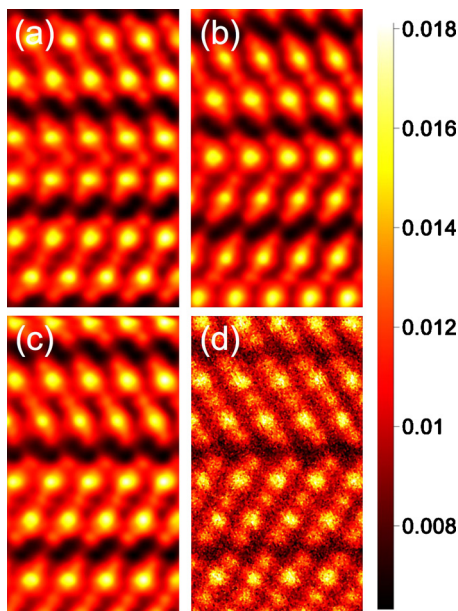


FIG. 4. (Color online) Simulated HAADF-STEM images for the three calculated twin terminations compared with experiment. (a) Twin 1: terminated at a  $\text{Te}^{(2)}$  layer. (b) Twin 2: terminated at a Bi layer. (c) Twin 3: terminated at a  $\text{Te}^{(1)}$  layer. (d) Experimental image. The simulations and experiment are presented on the same intensity scale. The contrast levels represent the recorded fraction of incident electron intensity. The experimental intensity was scaled as follows: a reference black level (or intensity level 0) was obtained from an experimental image of a hole in the sample, recorded with the same detector settings; the experimental gain value was calibrated by comparing the average intensity of the entire image from which (d) is cropped to the average simulated intensity of a large  $\text{Bi}_2\text{Te}_3$  supercell.

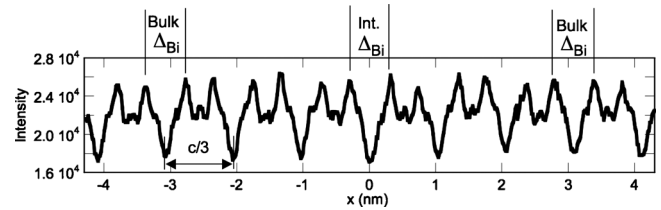


FIG. 5. Example of an intensity line profile collected from the HAADF-STEM images.

the recorded fraction of the incoming electron intensity. The intensity scale of the experimental image was calibrated from a reference experimental black level obtained in a hole in the sample and a reference intensity gain value was obtained by comparing the averaged experimental and simulated intensities for  $\text{Bi}_2\text{Te}_3$ .

The resulting simulated images are shown in Figs. 4(a)–4(c) in comparison with an experimental image in Fig. 4(d). The simulations show that the Te and Bi columns would be experimentally resolved for all three proposed structures and that the three possible boundary terminations are clearly distinguished. The good agreement between the experimental contrast and the simulation for the double  $\text{Te}^{(1)}$  structure shown in Fig. 4(c) confirms our interpretation of the micrographs.

We also measured the changes in interplanar spacing at the interface to compare with the predicted interfacial expansion for the structure of Twin 3. To make these measurements we determined the peak positions in intensity profiles extracted from the images. Each profile was constructed normal to the interface and integrated over 0.8 nm wide blocks. An example of one such profile is shown in Fig. 5. We determined the peak positions in these profiles by fitting a sum of Gaussians, of the form

$$I(x) = A_0 + \sum_{i=1}^5 A_i e^{[-(x - x_{0,i})^2 / 2\sigma_i^2]}, \quad (3)$$

to the five-layer quintet intensities. Here,  $A_i$  and  $\sigma_i$  are fitting constants,  $x$  is the position along the profile, and  $x_{0,i}$  is the position of the  $i$ th intensity peak.

From these measured peak positions, we determined the interplanar spacing between the  $\text{Te}^{(1)}$  layers across the interface ( $\Delta_{\text{Te,interface}}$ ) and between the Bi layers across the interface ( $\Delta_{\text{Bi,interface}}$ ) and compared these distances with equivalent measurements made in the bulk crystal (specifically across the third  $\text{Te}^{(1)}$ – $\text{Te}^{(1)}$  layer away from either side of the twin). The accuracy of the Bi measurements is better than that of the Te, since the Te intensities are lower and, therefore, show up as shoulders on the edge of the better defined Bi peaks. These results, compared with the equivalent distances computed from the relaxed structure for Twin 3, are shown in Table II. The measurements, from four different images, consistently show an expansion normal to the interface of  $0.012 \pm 0.004$  nm (0.009–0.015 nm across all four images; see Table II). This result is comparable with the *ab initio* calculations, which predict  $\Delta_{\text{Te,bulk}} - \Delta_{\text{Te,interface}} = 0.0120$  nm and  $\Delta_{\text{Bi,bulk}} - \Delta_{\text{Bi,interface}} = 0.0116$  nm.<sup>32</sup>



TABLE II. Experimentally measured expansions normal to the interface ( $\Delta_{\text{Te,bulk}} - \Delta_{\text{Te,interface}}$  and  $\Delta_{\text{Bi,bulk}} - \Delta_{\text{Bi,interface}}$ ).  $\Delta_{\text{Te,interface}}$  and  $\Delta_{\text{Bi,interface}}$  are, respectively, the  $\text{Te}^{(1)}\text{--Te}^{(1)}$  and Bi–Bi interplanar spacings measured across the Te double-layer at the interface. These distances are compared with the equivalent distances in the bulk of the crystal,  $\Delta_{\text{Te,bulk}}$  and  $\Delta_{\text{Bi,bulk}}$  (measured across the third double Te layer from either side the interface). The uncertainties in these measurements are quoted as the error of the mean,  $\sigma/\sqrt{N}$ , where  $\sigma$  is the standard deviation of the measurements and  $N$  is the number of measurements. These uncertainties are added in quadrature to give the uncertainty in the measured expansion.

Te <sup>(1)</sup> –Te <sup>(1)</sup> interplanar spacings					
Image	$\Delta_{\text{Te,bulk}}$ (nm)	$N$	$\Delta_{\text{Te,interface}}$ (nm)	$N$	$\Delta_{\text{Te,bulk}} - \Delta_{\text{Te,interface}}$ (nm)
1	$0.2710 \pm 0.0026$	30	$0.2846 \pm 0.0055$	15	$0.014 \pm 0.006$
2	$0.2666 \pm 0.0051$	34	$0.2818 \pm 0.0100$	17	$0.015 \pm 0.011$
3	$0.2640 \pm 0.0021$	20	$0.2732 \pm 0.0030$	10	$0.009 \pm 0.004$
4	$0.2778 \pm 0.0045$	36	$0.2881 \pm 0.0055$	18	$0.010 \pm 0.007$
Pooled	$0.2707 \pm 0.0022$	120	$0.2830 \pm 0.0036$	60	$0.012 \pm 0.004$
Twin 3 DFT-LDA	0.2530 (single crystal calculation)		0.2650		0.0120
Bi–Bi interplanar spacings					
Image	$\Delta_{\text{Bi,bulk}}$ (nm)	$N$	$\Delta_{\text{Bi,interface}}$ (nm)	$N$	$\Delta_{\text{Bi,bulk}} - \Delta_{\text{Bi,interface}}$ (nm)
1	$0.6054 \pm 0.0015$	30	$0.6203 \pm 0.0021$	15	$0.015 \pm 0.003$
2	$0.6046 \pm 0.0023$	34	$0.6149 \pm 0.0028$	17	$0.010 \pm 0.004$
3	$0.6104 \pm 0.0021$	20	$0.6204 \pm 0.0028$	10	$0.010 \pm 0.004$
4	$0.6125 \pm 0.0044$	36	$0.6274 \pm 0.0061$	18	$0.015 \pm 0.008$
Pooled	$0.6081 \pm 0.0016$	120	$0.6209 \pm 0.0022$	60	$0.013 \pm 0.003$
Twin 3 DFT-LDA	0.5965 (single crystal calculation)		0.6081		0.0116

#### IV. DISCUSSION

It is instructive to consider the qualitative factors controlling the interfacial energy for the three possible twin terminations in relationship to the perfect  $\text{Bi}_2\text{Te}_3$  structure. Here, we consider why the structure with the  $\text{Te}^{(1)}\text{--Te}^{(1)}$  termination has the lowest energy and what accounts for the relative energies of the other two structures.

In the case of the perfect  $\text{Bi}_2\text{Te}_3$  structure, the partial electronic density of states near the band gap is dominated by the contribution from  $p$ -orbitals.<sup>33–35</sup> Thus, a simple chemical bonding model for the five-layer unit can be constructed by neglecting the interunit interaction and considering only the  $pp\sigma$  intraunit interaction between neighboring atoms.<sup>33,34</sup> With each of the three  $p$ -orbitals on an atom pointing toward one atom on the layer above and one atom on the layer below, one obtains three independent (and nearly perpendicular) chains, each chain consisting of five  $p$ -orbitals interacting via the  $pp\sigma$  interaction. Within this simple model, a twin termination at the  $\text{Te}^{(1)}$  double-layer would have zero interfacial energy, making it the lowest energy structure of the three we considered. The other two possible twin structures would have higher energies than the perfect  $\text{Bi}_2\text{Te}_3$  structure because reversing the stacking at the  $\text{Te}^{(2)}$  or Bi layer does not allow a pure  $pp\sigma$  interaction between an atom in the interface layer and a neighbor atom from an adjacent layer (simply because the five-atom chains cannot follow a straight line across the interface).

The contribution to the interfacial energy in the *ab initio* calculations comes mainly from structural relaxations near the interface. One expects that the most affected interlayer interaction is the one between the interface layer and the

adjacent (below and above) layers. Based on the interatomic distance between neighboring atoms in the five-layer unit of the perfect  $\text{Bi}_2\text{Te}_3$  structure, the bond between  $\text{Te}^{(1)}$  and Bi (our theoretical interatomic distance in the perfect  $\text{Bi}_2\text{Te}_3$  structure is  $d_{\text{Te}^{(1)}\text{--Bi}} = 0.304$  nm) is stronger than the one between  $\text{Te}^{(2)}$  and Bi ( $d_{\text{Te}^{(2)}\text{--Bi}} = 0.320$  nm). One then expects that placing the twin interface at the  $\text{Te}^{(2)}$  layer (Twin 1) will result in a lower energy than placing it at the Bi layer (Twin 2), because it is in the latter case that the stronger  $\text{Te}^{(1)}\text{--Bi}$  bond is most altered. Indeed, we find through our *ab initio* structural calculations that the  $\text{Te}^{(2)}\text{--Bi}$  bond at the interface of Twin 1 is 0.0028 nm longer than in the perfect  $\text{Bi}_2\text{Te}_3$  structure. In contrast, for the case of a twin interface at the Bi layer (Twin 2), the  $\text{Te}^{(2)}\text{--Bi}$  and  $\text{Te}^{(1)}\text{--Bi}$  bonds at the interface are longer than in the perfect  $\text{Bi}_2\text{Te}_3$  structure by 0.0093 nm and 0.0035 nm, respectively, indicating a stronger distortion of the interlayer interaction across the interface than for the  $\text{Te}^{(2)}$  interface (Twin 1).

We note that the calculated energy of the twin terminated at the  $\text{Te}^{(1)}$  layer (Twin 3) is not much lower than that of the twin terminated at the  $\text{Te}^{(2)}$  layer (Twin 1). This relatively high energy is consistent with the elongation of the  $\text{Te}^{(1)}\text{--Te}^{(1)}$  bond at the interface of Twin 3 (which we calculate is 0.0088 nm longer than in the perfect  $\text{Bi}_2\text{Te}_3$  structure). While commonly considered as a weak, van der Waals interaction, the  $\text{Te}^{(1)}\text{--Te}^{(1)}$  bond in  $\text{Bi}_2\text{Te}_3$  has been found to be stronger than typical van der Waals interactions.<sup>35</sup> We believe this is at the origin of the relatively high interfacial energy we calculate for Twin 3. However, it is also possible that use of the LDA in the DFT implementation may overestimate the strength of the  $\text{Te}^{(1)}\text{--Te}^{(1)}$  bond more than it



does for the other, stronger bonds ( $pp\sigma$ ) because nonlocal electron correlations, which are important for a correct description of the van der Waals interaction,<sup>36</sup> are not accounted for within the LDA.

## V. CONCLUSIONS

In summary, we have determined the structure of the (0001) basal twin in  $\text{Bi}_2\text{Te}_3$ . Our HAADF-STEM observations and *ab initio* calculations show that the reversal of basal plane stacking occurs at the  $\text{Te}^{(1)}$  layers. This termination is consistent with the bonding picture for  $\text{Bi}_2\text{Te}_3$ , where the  $\text{Te}^{(1)}-\text{Te}^{(1)}$  layers are thought to be bonded through relatively weak, van der Waals-type interactions. In contrast, the other two possible twin terminations, namely, at the Bi or  $\text{Te}^{(2)}$  layers, would require a distortion of the linear chains of  $pp\sigma$  bonds within the middle of the  $\text{Bi}_2\text{Te}_3$  five-layer pack-ets.

The variation in bonding between the different layers of  $\text{Bi}_2\text{Te}_3$ , and the corresponding dependence of the twin boundary energy on the twin boundary plane, raises interesting questions concerning the mechanisms by which the twins form. In general, for a twin to propagate, each of the adjacent atomic layers must shear or shuffle to reverse its local stacking arrangement. For instance, in face centered cubic metals, this process occurs through the motion of Shockley partial dislocations. Although shear across the  $\text{Te}^{(1)}-\text{Te}^{(1)}$  layers may occur with little energetic penalty, the barriers will likely be higher for the continued shear of the Bi and  $\text{Te}^{(2)}$  layers, since the  $pp\sigma$  bonds must be distorted for the twin to propagate. Establishing the mechanisms by which this propagation occurs may yield routes to better control and tailor the formation of twins in  $\text{Bi}_2\text{Te}_3$ -based compounds.

## ACKNOWLEDGMENTS

Sandia is a multiprogram laboratory operated by Sandia Corporation, a Lockheed-Martin Co., for the U.S. DOE-NNSA, under Contract No. DE-AC04-94AL85000. Support at Sandia was provided in part by the Office of Basic Energy Sciences, Division of Materials Sciences, of the U.S. Department of Energy. The authors acknowledge the user program of the National Center for Electron Microscopy, Lawrence Berkeley National Laboratory, which is supported by the Office of Science, Office of Basic Energy Sciences of the U.S. Department of Energy under Contract No. DE-AC02-05CH1123. The authors are grateful to Dr. Zhihui Zhang and Professor Enrique Lavernia, University of California, Davis, for assistance with the spark plasma sintering, and to Mr. Mark Homer, for preparing the TEM specimens.

<sup>1</sup>D. M. Rowe, *Thermoelectrics Handbook: Macro to Nano* (CRC, Boca Raton, FL, 2006).

<sup>2</sup>G. S. Nolas, J. Sharp, and H. J. Goldsmid, *Thermoelectrics: Basic Principles and New Materials Developments* (Springer-Verlag, Berlin, 2001).

- <sup>3</sup>B. Poudel, Q. Hao, Y. Ma, Y. Lan, A. Minnich, B. Yu, X. Yan, D. Wang, A. Muto, D. Vashaee, X. Chen, J. Liu, M. S. Dresselhaus, G. Chen, and Z. Ren, *Science* **320**, 634 (2008).
- <sup>4</sup>W. Xie, X. Tang, Y. Yan, Q. Zhang, and T. M. Tritt, *J. Appl. Phys.* **105**, 113713 (2009).
- <sup>5</sup>X. Ji, J. He, Z. Su, N. Gothard, and T. M. Tritt, *J. Appl. Phys.* **104**, 034907 (2008).
- <sup>6</sup>S. Tsunekawa, K. Kido, and T. Watanabe, *Philos. Mag. Lett.* **85**, 41 (2005).
- <sup>7</sup>Z.-J. Wang, S. Tsunekawa, K. Ikeda, T. Sekiguchi, and T. Watanabe, *Interface Sci.* **7**, 197 (1999).
- <sup>8</sup>J. Chen, D. Yang, Z. Xi, and T. Sekiguchi, *J. Appl. Phys.* **97**, 033701 (2005).
- <sup>9</sup>B. A. Cook, M. J. Kramer, X. Wei, J. L. Harringa, and E. M. Levin, *J. Appl. Phys.* **101**, 053715 (2007).
- <sup>10</sup>D. L. Medlin and G. J. Snyder, *Curr. Opin. Colloid Interface Sci.* **14**, 226 (2009).
- <sup>11</sup>J. W. Christian and S. Mahajan, *Prog. Mater. Sci.* **39**, 1 (1995).
- <sup>12</sup>S. Mahajan, C. S. Pande, M. A. Iman, and B. B. Rath, *Acta Mater.* **45**, 2633 (1997).
- <sup>13</sup>J. Seo, D. Lee, C. Lee, and K. Park, *J. Mater. Sci. Lett.* **16**, 1153 (1997).
- <sup>14</sup>J. Seo, C. Lee, and K. Park, *J. Mater. Sci.* **35**, 1549 (2000).
- <sup>15</sup>S. Miura, Y. Sato, K. Fukuda, K. Nishimura, and K. Ikeda, *Mater. Sci. Eng., A* **277**, 244 (2000).
- <sup>16</sup>J. T. Im, K. T. Hartwig, and J. Sharp, *Acta Mater.* **52**, 49 (2004).
- <sup>17</sup>O. Ben-Yehuda, R. Shuker, Y. Gelbstein, Z. Dashevsky, and M. P. Dariel, *J. Appl. Phys.* **101**, 113707 (2007).
- <sup>18</sup>Y. Q. Cao, X. B. Zhao, T. J. Zhu, X. B. Zhang, and J. P. Tu, *Appl. Phys. Lett.* **92**, 143106 (2008).
- <sup>19</sup>J. R. Wiese and L. Muldrew, *J. Phys. Chem. Solids*, **15**, 13 (1960).
- <sup>20</sup>S. Nakajima, *J. Phys. Chem. Solids* **24**, 479 (1963).
- <sup>21</sup>A. Adam, *Mater. Res. Bull.* **42**, 1986 (2007).
- <sup>22</sup>J. L. Lensch-Falk, J. D. Sugar, M. A. Hekmaty, and D. L. Medlin, *J. Alloys Compd.* (in press).
- <sup>23</sup>C. Kisielowski, B. Freitag, M. Bischoff, H. van Lin, S. Lazar, G. Knippels, P. Tienmeijer, M. van der Stam, S. von Harrach, M. Stekelenburg, H. Haider, S. Uhlemann, H. Müller, P. Hartel, B. Kabius, D. Miller, I. Petrov, E. A. Olson, T. Donchev, E. A. Kenik, A. R. Lupini, J. Bentley, S. J. Pennycook, I. M. Anderson, A. M. Minor, A. K. Schmid, T. Duden, V. Radmilovic, Q. M. Ramasse, M. Watanabe, R. Erni, E. A. Stach, P. Denes, and U. Dahmen, *Microsc. Microanal.* **14**, 469 (2008).
- <sup>24</sup>W. Kohn and L. J. Sham, *Phys. Rev.* **140**, A1133 (1965).
- <sup>25</sup>N. Troullier and J. L. Martins, *Phys. Rev. B* **43**, 1993 (1991).
- <sup>26</sup>S. G. Louie, S. Froyen, and M. L. Cohen, *Phys. Rev. B* **26**, 1738 (1982).
- <sup>27</sup>H. J. Monkhorst and J. D. Pack, *Phys. Rev. B* **13**, 5188 (1976).
- <sup>28</sup>N. Frangis, S. Kuypers, C. Manolikas, G. Van Tendeloo, J. Van Landuyt, and S. Amelinckx, *J. Solid State Chem.* **84**, 314 (1990).
- <sup>29</sup>N. D. Browning, D. J. Wallis, P. D. Nellist, and S. J. Pennycook, *Micron* **28**, 333 (1997).
- <sup>30</sup>C. T. Koch, Ph.D. thesis, Arizona State University, 2002.
- <sup>31</sup>R. Egerton, *Electron Energy-Loss Spectroscopy in the Electron Microscope* (Plenum, New York, 1996).
- <sup>32</sup>The *ab initio* calculations predict a slightly smaller c-axis for the bulk single crystal (2.983 nm) compared to experiments (3.050 nm), due to the LDA implementation of DFT, which in general underestimates the crystal volume of bulk materials (LDA tends to overestimate the bonding). We ignore this difference, which is about 2.2%, in our comparisons of the relaxations since it is small compared with the uncertainty in our measurements.
- <sup>33</sup>P. Pecher and G. Toussaint, *Phys. Lett. A* **135**, 223 (1989).
- <sup>34</sup>S. K. Mishra, S. Satpathy, and O. Jepsen, *J. Phys.: Condens. Matter* **9**, 461 (1997).
- <sup>35</sup>B.-L. Huang and M. Kaviani, *Phys. Rev. B* **77**, 125209 (2008).
- <sup>36</sup>D. C. Langreth, B. I. Lundqvist, S. D. Chakarova-Käck, V. R. Cooper, M. Dion, P. Hyldgaard, A. Kelkkanen, J. Kleis, L. Kong, S. Li, P. G. Moses, E. Murray, A. Puzder, H. Rydberg, E. Schröder, and T. Thonhauser, *J. Phys.: Condens. Matter* **21**, 084203 (2009).